Int J Adv Manuf Technol (2015) 80:2083–2096
DOI 10.1007/s00170-015-7156-5

ORIGINAL ARTICLE

A hybrid analytical- and discrete-based methodology for determining cutter-workpiece engagement in five-axis milling

Gandjar Kiswanto[1] · **Hendriko Hendriko**[1,2,3] · **Emmanuel Duc**[2]

Received: 13 August 2014 / Accepted: 12 April 2015 / Published online: 1 May 2015

Abstract This paper presents a new method to determine the cutter-workpiece engagement (CWE) for a toroidal cutter during free-form surface machining in five-axis milling. A hybrid method, which is a combination of a discrete model and an analytical approach, was developed. Although the workpiece surface was discretized by a number of normal vectors, there was no calculation to determine the intersection between the normal vector and the cutting tool. The normal vectors were used to define the workpiece surface mathematically; next, the engagement point was calculated using a combination of the workpiece surface equation, the parametric equation of the cutting tool, and the tool orientation data. Three model parts with different surface profiles were tested to verify the validity of the proposed method; the results indicated that the method was accurate. The method also eliminated the need for a large number of discrete vectors to define the workpiece surface. A comparison showed that the proposed method was computationally more efficient. The CWE model was subsequently applied to support the cutting force prediction model. A validation test demonstrated that in terms of trends and amplitudes, the predicted cutting forces exhibit good agreement with the cutting force generated experimentally.

✉ Gandjar Kiswanto
gandjar_kiswanto@eng.ui.ac.id

[1] Laboratory of Manufacturing Technology and Automation, Department of Mechanical Engineering, Universitas Indonesia, Depok, Indonesia

[2] IFMA, UMR 6602, Institut Pascal, Clermont Université, BP 10448, F-63000 Clermont-Ferrand, France

[3] Mechatronics Department, Politeknik Caltex Riau, Pekanbaru, Indonesia

Keywords Five-axis milling · Analytical method · Cutter-workpiece engagement

1 Introduction

In theory, the five-axis machining of sculptured surfaces with toroidal cutter can provide many advantages, including the acceleration of material removal rates, the improvement of surface finishes, and the elimination of hand finishing, compared to three-axis machining with a ball end-mill [1]. Currently, the ability of a system to generate an optimal process plan automatically is an essential step of achieving automation, higher productivity, and better accuracy [2]. Various studies [2–5] have been performed to develop a new approach called virtual machining. The primary purposes of virtual machining in a milling operation include how to predict the instantaneous cutting force and the surface roughness, which can be used as inputs to shorten machining time by optimizing process parameters without sacrificing machining quality.

To support machining optimization, precise geometric information is required, particularly during modeling and when calculating the cutting force [6]. Many studies of the geometric simulation strategy based on solid modeling including constructive solid geometry (CSG) and boundary representations (B-Rep) have been conducted. Altintas and Spence [7, 8] used CSG to identify the cutter-workpiece intersection to predict cutting forces, while Fleisig and Spence [9] used B-Rep-based machining simulations for rough machining of 2.5D pockets. Other researchers who have contributed significantly include Jerard et al. [10], who evaluated the conditions of cutter-part engagement with computationally efficient algorithms called the Z-map method. In this method, the workpiece was discretized into a set of evenly distributed discrete z-direction vectors (ZDV). The Z-map or dexel can be thought

of as a special type of discrete vector model or a discrete vector [11–17]. Solid modeling yields more accurate information but requires significantly more computation time. Additionally, the discrete vector model improves calculation speeds compared to solid modeling; however, the computation time and memory consumption increases significantly because the precision and accuracy is also significantly improved.

To overcome such problems, Ozturk and Lazoglu [18] proposed an analytical method to determine the chip load of a ball end-mill during free-form machining. The chip load was determined by defining three engagement boundaries: the tool entry boundary, the exit boundary, and the workpiece surface boundary. Song et al. [19] used an analytical method to calculate the instantaneous undeformed chip thickness based on the true trochoid path of the tool tooth. Although these methods were fast and accurate, they were only applicable to three-axis milling. Another study was performed by Tunc and Budak [20], who used a simple analytical method called the bounding point coordinate method applied to five-axis milling. Using this method, the depth of each cut in each tool location can be predicted by defining the coordinate of the cutter contact point. The tests showed that the proposed method could predict the depth of a cut accurately. However, this technique is only applicable for flat workpiece surfaces. When the workpiece surface was a free-form surface, the authors of that study used a discretization method to represent the workpiece surface. Kiswanto et al. [21] proposed an analytical method called the Analytical Boundary Simulation to define the cutter-workpiece engagement (CWE) in five-axis milling. The proposed method was proven accurate and faster than Z-mapping method; however, the method was only applicable to semi-finishing processes using a workpiece with a straight staircase surface profile. Gupta et al. [22] also mentioned that analytical approaches for computing cutter engagement were much faster and more accurate compared to discrete approaches. Although the analytical methods were preferable to discrete methods, studies of the analytical methods have not been developed.

This paper presents a hybrid method to calculate the CWE between a toroidal cutter and a free-form workpiece surface. The proposed method was a combination of the analytical method and the discrete-vector-based methodology, in which discrete normal vectors were used to describe the workpiece surface. Despite the normal vectors used in this model, there was no calculation to determine the contact between the cutter and the normal vector. The coordinate of the normal vector and its orientation were used to define the shape of the surface at every tool position mathematically. In this study, the CWE was determined by defining two engagement points, as shown in Fig. 1; these include the lowermost engagement point (LE point), which is represented by C, and the uppermost engagement point (UE point), which is denoted by n_f. After obtaining these two points, the length of each cut at every engagement angle can be calculated. The LE point was calculated using the grazing method described in [21] and will not be discussed in this paper. A flow chart describing the steps used to obtain the LE point and the UE point are presented in Fig. 2; additional details will be given in subsequent sections of this paper.

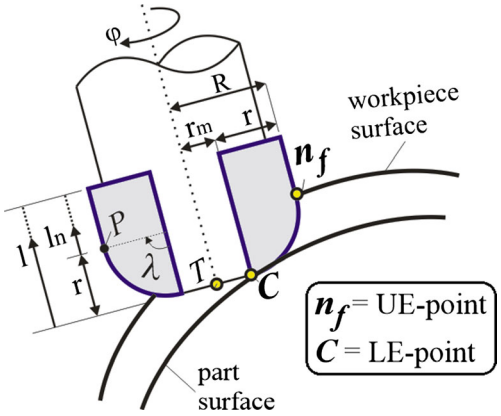

Fig. 1 Geometry of a toroidal cutter and its cutter-part engagement points

2 Identifying the instantaneous surface shape

As mentioned in the introduction, the method proposed in this study is a combination of discretization and the analytical method. The normal vectors are distributed on the workpiece surface, as shown in Fig. 3a. Compared to the fully discrete method, the proposed method uses a smaller number of normal vectors to represent the workpiece surface. The normal vectors contain information about the workpiece surface including its coordinates, its orientation relative to the workpiece coordinate system (WCS) about the x-axis (μ_x), and that about the y-axis (μ_y), as shown in Fig. 3b.

A small portion of the workpiece surface, as illustrated in Fig. 3a, was approximated by a surface that was a combination of the surface shape in the x-axis (S_x) and the y-axis (S_y), as illustrated in Fig. 3c. The shape of the surface can be a combination of a convex, concave, flat, or sloped surface. This approximation was used to define the shape of the workpiece surface at an instantaneous tool location.

Figure 4a shows a top view of the workpiece surface. The shape of an instantaneous workpiece surface region was defined using three selected normal vectors (v_1, v_2, v_3), where v_1 was a reference vector that was located closest to the LE point, which could be located inside or outside the cutter region, while v_2 and v_3 were the vectors that are located before v_1.

Based on the coordinates and orientation of the normal vectors, the radius of the workpiece surface in the x-axis (R_x)

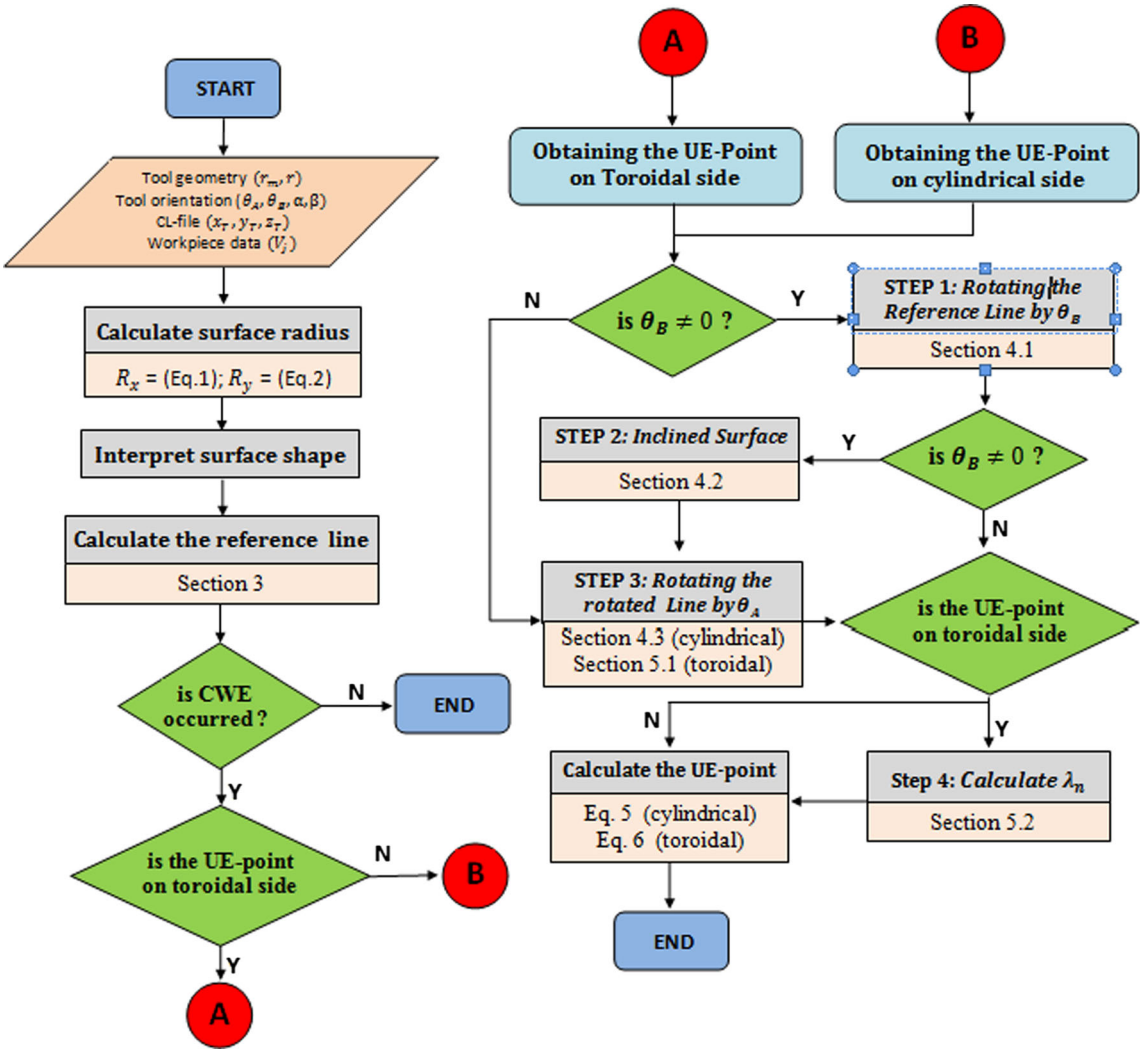

Fig. 2 Flow chart to obtain the UE point

was determined using Eq. 1; these equations were derived by referring to Fig. 4b. Using the same method, the radius of the workpiece surface in the y-axis (R_y) was determined using Eq. 2:

$$R_x = \left(\sqrt{(x_2-x_1)^2 + (z_2-z_1)^2}\right)/(2\ \sin(0.5(\mu_{x2}-\mu_{x1}))) \quad (1)$$

$$R_y = \left(\sqrt{(y_3-y_1)^2 + (z_3-z_1)^2}\right)/\left(2\ \sin\left(0.5\left(\mu_{y2}-\mu_{y1}\right)\right)\right) \quad (2)$$

After R_x and R_y were obtained, several conclusions regarding the shape of the workpiece surface in the x-axis (S_x) and the y-axis (S_y) could be made:

- Convex surface: if $R_x>0, R_y>0$
- Concave surface: if $R_x<0, R_y<0$
- Flat surface: if $R_x=0$ and $\mu_{x1}=0$; or $R_y=0$ and $\mu_{y1}=0$
- Slope surface: if $R_x=0$ and $\mu_{x1}\neq 0$, slope angle (γ) $=\mu_{x1}$; or $R_x=0$ and $\mu_{y1}\neq 0$, $\gamma=\mu_{y1}$

Then, the shape of an instantaneous workpiece surface (i.e., a surface region) was constructed using a combination of S_x and S_y; several feasible combinations are shown in Fig. 3c.

The method to identify the selected normal vectors, as illustrated in Fig. 4a, was applied when the shape of the workpiece surface at the instantaneous tool location was determined using only one surface region. When the workpiece surface had a higher curvature, the shape of the instantaneous surface could be very complex, and the errors could be higher if only one surface region were used to represent the instantaneous workpiece surface. Because the accuracy of this method was significantly influenced by the accuracy in determining the shape of the workpiece surface, the instantaneous workpiece surface was divided into two or more regions instead of

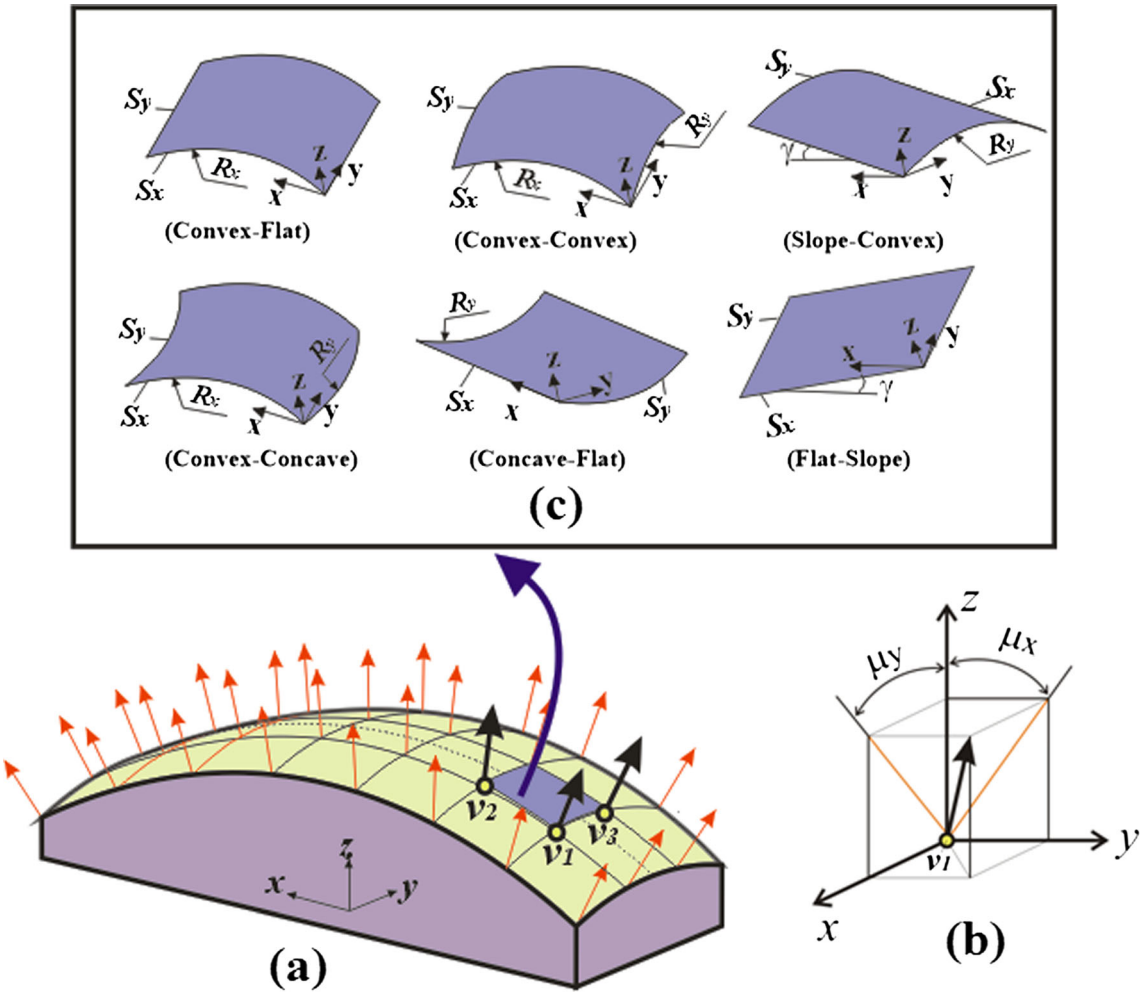

Fig. 3 Workpiece surface representation: **a** normal vector distribution, **b** vector orientation in WCS, and **c** feasible surface shape combinations

one region; this would reduce the error due to the complexity of the surface. The method to define the shape of the surface for each region was similar to that previously discussed. When the surface was separated into several regions, the workpiece surface should be discretized with a larger number of normal vectors, as illustrated in Fig. 4c.

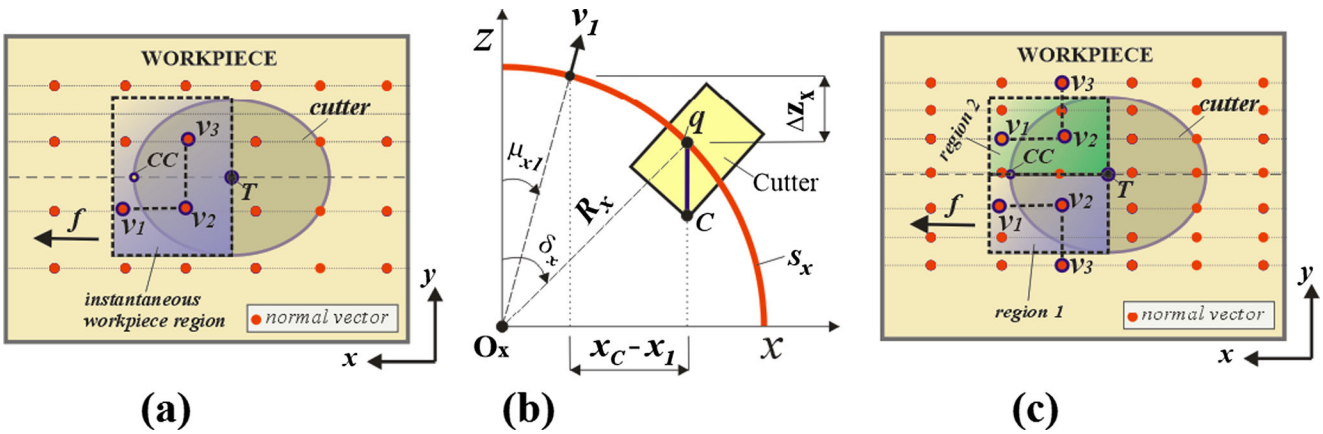

Fig. 4 Workpiece surface representation: **a** discretization method with a single surface region, **b** method to calculate the radius of the workpiece surface, and **c** discretization method with more surface regions

3 Checking the feasible engagement location

In this study, the method was developed for a toroidal cutter, which can be decomposed into cylindrical (G_C) and toroidal (G_T) surfaces, as depicted in Fig. 1; these surfaces were defined using the following equations:

$$G_C(\varphi; l_k) = [\,(r_m + r)\sin\varphi \quad (r_m + r)\cos\varphi \quad l\,]^{\mathrm{T}} \tag{3}$$

$$G_T(\varphi; \lambda) = [\,(r_m + r\sin\lambda)\sin\varphi \quad (r_m + r\sin\lambda)\cos\varphi \quad r - r\cos\lambda\,]^{\mathrm{T}} \tag{4}$$

where r is the minor radius of cutting tool, r_m is the distance between the cutter center point to the minor radius, l is the height of the cutter measured from its tip, and λ and φ denote the toroidal angle and the engagement angle, respectively.

In five-axis milling, the cutting tool can be oriented in any direction, and the orientation of the cutting tool relative to the workpiece coordinate system (WCS) can be described using the tool rotation about the x-axis (θ_A) and the y-axis (θ_B). Because the cutter contact (CC) data and the workpiece surface information were provided in the WCS, the cutter surfaces were transformed from the tool coordinate system (TCS) into the WCS. Then, Eqs. 3 and 4 yielded:

$$G_C'\left(x'_{S_C},\, y'_{S_C}, z'_{S_C}\right) = [\mathrm{M}]G_C(\varphi; l) \tag{5}$$

$$G_T'\left(x'_{S_T},\, y'_{S_T}, z'_{S_T}\right) = [\mathrm{M}]G_T(\varphi; \lambda) \tag{6}$$

where [M] is the operator that maps the coordinate system from the TCS to the WCS involving the tool rotation about the x-axis (θ_A), the y-axis (θ_B), and the translation at T, where $T(x_T, y_T, z_T)$ is the cutter location point (i.e., CL point) that is located at the bottom center of cutting tool:

$$[\mathrm{M}] = \begin{bmatrix} \cos\theta_B & 0 & \sin\theta_B & x_T \\ \sin\theta_A\sin\theta_B & \cos\theta_A & -\sin\theta_A\cos\theta_B & y_T \\ \cos\theta_A\sin\theta_B & \sin\theta_A & \cos\theta_A\cos\theta_B & z_T \\ 0 & 0 & 0 & 1 \end{bmatrix} \tag{7}$$

Because the generic equations for the toroidal and cylindrical sides of the cutting tool are different, the method to calculate the UE point on the toroidal side was different than that on the cylindrical side. Therefore, whether the CWE exists or not should be determined in the beginning. If the CWE exists, then whether the CWE is located on the toroidal side or on the cylindrical side should be determined. This check step was performed by calculating the projection lines, $\overline{Cw_c}$, and $\overline{Cw_p}$, as depicted in Fig. 5.

Before defining $\overline{Cw_c}$ and $\overline{Cw_p}$, the coordinate of w_C $\left(x_{w_C}, y_{w_C}, z_{w_C}\right)$ and $w_p\left(x_{w_p}, y_{w_p}, z_{w_p}\right)$ should be determined. Because w_C and w_p were the points projected from point $C(x_C, y_C, z_C)$ and point $P(x_P, y_P, z_P)$, respectively, $\left\{x_{w_C}, y_{w_C}, x_{w_p}, y_{w_p}\right\}$ were equal to $\{x_C, y_C, x_p, y_p\}$. Thus, z_{w_C} could be obtained by calculating the distance in the z-axis between v_1 and w_C on $S_x(-\Delta Z_x)$ and the z-axis on S_y with respect to $y_c(\Delta Z_y)$ First, by working on S_x, the z value was calculated by comparing x_C with the coordinates and orientation of the reference vector v_1. The equations to obtain (ΔZ_x) and (ΔZ_y) for a curved surface (concave or convex) were expressed by:

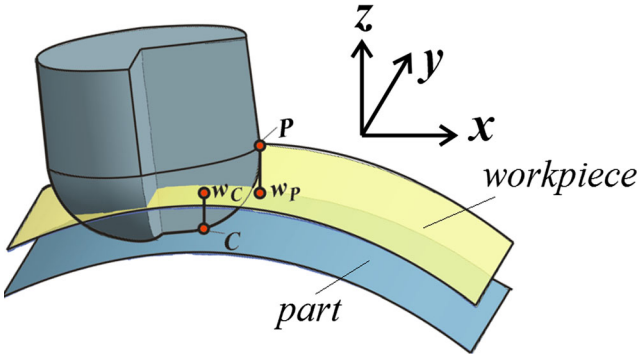

Fig. 5 Two projection lines

$$\begin{aligned} \Delta Z_x &= R_x\left(\ \cos\left(\sin^{-1}\left((R_x\sin\varepsilon_{x1} + (x_C - x_1))/R_x\right)\right) - \cos\varepsilon_{x1}\right); \\ \Delta Z_y &= R_y\left(\ \cos\sin^{-1}\left(\left(R_y\sin\varepsilon_{y1} + (y_C - y_1)\right)/R_y\right) - \cos\varepsilon_{y1}\right) \end{aligned} \tag{8}$$

For a flat or sloped surface, these values were determined by Eqs. 9 and 10, respectively:

$$\Delta Z_x = 0 \ \text{ and } \ \Delta Z_y = 0 \tag{9}$$

$$\Delta Z_x = (x_C - x_1)\tan\varepsilon_{x1};\ \Delta Z_y = (y_C - y_1)\tan\varepsilon_{y1} \tag{10}$$

Finally, z_{w_C} was defined as follows:

$$z_{w_C} = z_1 + \Delta Z_x + \Delta Z_y \tag{11}$$

After z_{w_C} was determined, the length of the projection line from C to w_C was calculated by $\overline{Cw_c} = z_{w_C} - z_C$. Using the same procedures, the line $\overline{Pw_p}$ was determined. The projection lines, $\overline{Cw_c}$ and $\overline{Pw_c}$, were used to define the location of the UE point by following the rules below:

1. If $\overline{Cw_c} > 0$ and $\overline{Cw_p} \le 0$, then the UE point was located on the toroidal side, and $\overline{Cw_c}$ was selected as the reference line $\overline{(Cq)}$.
2. If $\overline{Cw_c} > 0$ and $\overline{Cw_p} > 0$, then the UE point was located on the cylindrical side, and $\overline{Pw_p}$ was selected as the reference line $\overline{(Cq)}$.
3. If $\overline{Cw_c} < 0$ and $\overline{Cw_p} < 0$, there was no engagement between the cutter and the workpiece.

The reference line is a line that will be used as a reference to calculate the length of each cut and to define the coordinate of the CWE.

4 Obtaining the UE point on the cylindrical side

After the reference line was determined, it was then rotated using the tool orientation angles (θ_B and θ_A) to obtain the UE point. These two rotation procedures must be performed sequentially except in certain conditions when it can be skipped, and the next procedure may begin. In this section, the detailed procedure of determining the UE point located on the cylindrical side is derived.

4.1 Step 1: rotating the projection line by θ_B

In the first step, to determine the line $\overline{Cs}$, the reference line was rotated about the point (C, θ_B). If θ_B was equal to zero, then the line $\overline{Cs}$ was equal to the line $\overline{Cq}$. The equations to define the rotated line for every surface shape are shown below. For a convex surface, the equations were determined by Fig. 6a and are expressed as follows:

$$\overline{CO_x} = \left(\overline{Cq^2} + R_x^2 - 2\overline{Cq}R_x\cos\delta_x\right)^{0.5} \tag{12}$$

$$\phi_b = 180 - |\theta_B| - \left|\delta_x + \cos^{-1}\left(\left(\overline{CO_x}^2 + R_x^2 - \overline{Cq^2}\right)\Big/\left(2\,\overline{CO_x}R_x\right)\right)\right| \tag{13}$$

$$\phi_c = \sin\left(\overline{CO_x}\sin\phi_b / R_x\right) \tag{14}$$

$$\overline{Cs} = \left(R_x^2 + \overline{CO_x}^2 - 2R_x^2\overline{CO_x}^2\cos(180 - \phi_b - \phi_c)\right)^{0.5} \tag{15}$$

For a concave surface, the equations to calculate the line $\overline{Cs}$ were developed using Fig. 6b and are calculated as follows:

$$\overline{CO_x} = \left(\overline{Cq}^2 + R_x^2 - 2\overline{Cq}R_x\cos\delta_x\right)^{0.5} \tag{16}$$

$$\phi_b = \left|\theta_B - \sin^{-1}\left(R_x^2\sin(180 - \delta_x)/\overline{CO_x}\right)\right| \tag{17}$$

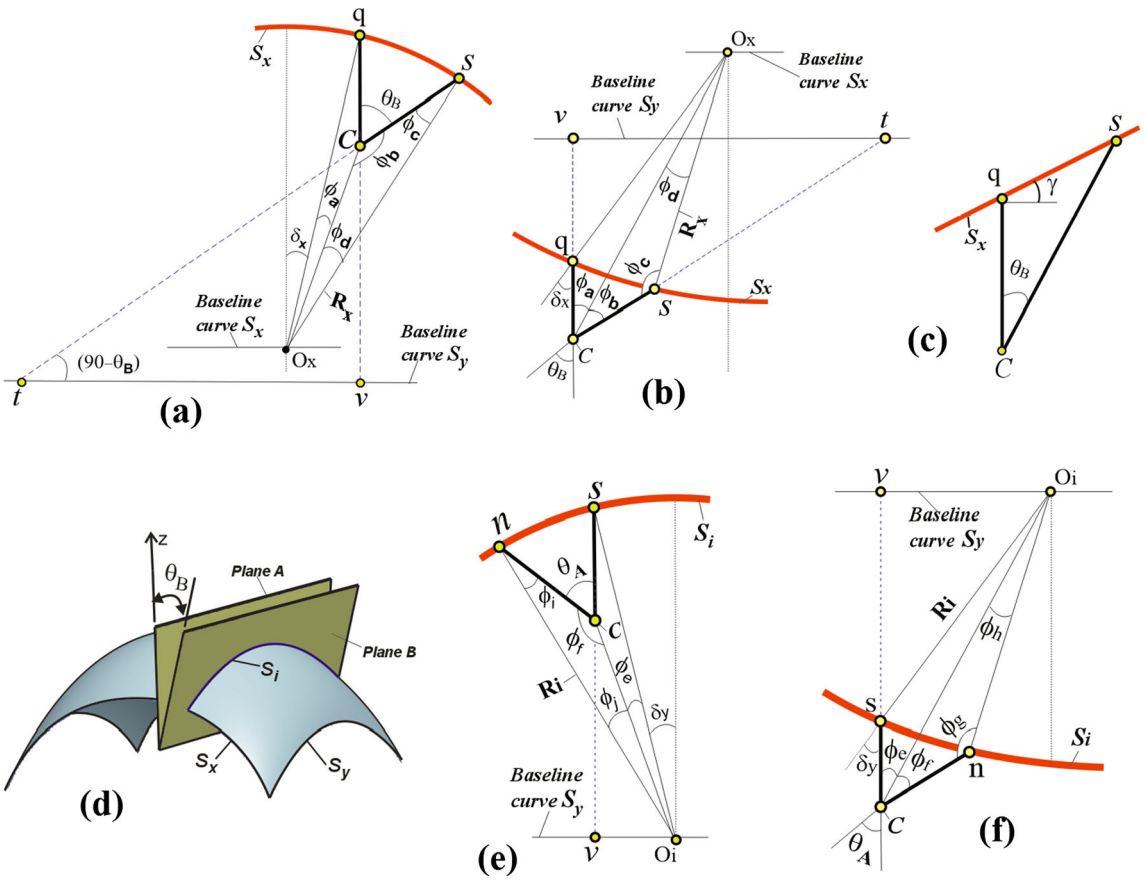

Fig. 6 Rotation of the projection line on S_x: **a** convex surface, **b** concave surface, **c** slope surface, **d** inclined surface, **e** rotation of rotated reference line of a convex surface on S_i, and **f** for a concave surface

$$\phi_c = 180 - \sin^{-1}\left(\overline{CO_{x2}}\sin\phi_b / R_x\right) \tag{18}$$

$$\overline{Cs} = \left(R_x^2 + \overline{CO_{x2}}^2 - 2R_x^2\overline{CO_{x2}}^2\cos\left(180 - \phi_b - \phi_c\right)\right)^{0.5} \tag{19}$$

More simple equations were used to calculate the line $\overline{Cs}$ for a slope surface and a flat surface as depicted in Eqs. 20 and 21, respectively. For a slope surface, the equation was derived by referring to Fig. 6c.

$$\overline{Cs} = \overline{Cq}\sin(90+\gamma)/\sin(90 - \gamma - \theta_B) \tag{20}$$

$$\overline{Cs} = \overline{Cq}/\cos\theta_B$$

4.2 Step 2: calculating the radius of the inclined surface

If θ_B was not equal to zero, then the reference line was rotated in the first step. Due to this rotation, the reference line was not perpendicular to the second surface (S_y). Consequently, when S_y was a curved surface, the line $\overline{Cs}$ could not be mapped or rotated on S_y due to the line $\overline{Cs}$ and the surface S_y were no longer aligned; this phenomenon is exhibited in Fig. 6d. The inclined curved surface S_i was determined by slicing the workpiece material using plane B. Plane B began as plane A and was rotated by θ_B. The radius of S_i (R_i) was dependent on S_x. When S_x was a curved surface, the equations were derived based on Fig. 6a. Line $\overline{qv}$ is the distance along the z-axis from a projected point q on the workpiece surface to the baseline of curved surface S_y. The radius of S_i for every surface shape was calculated using the following equations:

$$R_i = \left(\left(\left(R_y\cos\delta_y - \overline{Cq}\right)/\cos\theta_x\right) + \overline{Cs}\right)^2 + \left(R_y\sin\delta_y\right)^2\Big)^{0.5}; \rightarrow \text{convex} \tag{22}$$

$$R_i = \left(\left(\left(R_y\cos\delta_y + \overline{Cq}\right)/\cos\theta_x\right) - \overline{Cs}\right)^2 + \left(R_y\sin\delta_y\right)^2\Big)^{0.5}; \rightarrow \text{concave} \tag{23}$$

$$R_i = \left(R_y\sin(90+\gamma)\right)/\sin(90 - \gamma - \theta_B); \rightarrow \text{slope} \tag{24}$$

$$R_i = R_y/\cos\theta_B; \rightarrow \text{flat} \tag{25}$$

R_i was calculated only if it met three conditions: θ_B, R_y, and θ_A were not equal to zero; otherwise, $R_i = R_y$.

4.3 Step 3: rotating the rotated line by θ_A

In step 3, the rotated reference line $\overline{C\,s}$ from step 1 was rotated again about point C by θ_A. This rotation procedure attempted to obtain the line $\overline{C\,n}$ on S_i. This step was performed only if θ_A was not equal to zero; otherwise, $\overline{C\,n} = \overline{C\,s}$. For a convex surface, the equations to calculate $\overline{C\,n}$ were derived by referring to Fig. 6e:

$$\overline{C\,O_i} = \left(\overline{C\,s}^2 + R_i^2 - 2\overline{C\,s}R_i\cos\delta_y\right)^{0.5} \tag{26}$$

$$\phi_f = 180 - |\theta_y| - |\delta_Y| + \cos^{-1}\left(\left(\overline{C\,O_i}^2 + R_i^2 - \overline{C\,s}^2\right)/\left(2\overline{C\,O_i}R_i\right)\right) \tag{27}$$

$$\phi_g = \sin\left(\overline{C\,O_i}\sin\phi_f / R_i\right); \tag{28}$$

$$\overline{C\,n} = \left(R_i^2 + \overline{C\,O_i}^2 - 2R_i\overline{C\,O_i}\cos\left(180 - \left(\phi_f + \phi_g\right)\right)\right)^{0.5} \tag{29}$$

For a concave surface, the method was derived by referring to Fig. 6f, and the results were calculated as follows:

$$\overline{C\,O_i} = \left(\overline{C\,q}^2 + R_i^2 - 2\overline{C\,q}R_i\cos\delta_y\right)^{0.5} \tag{30}$$

$$\phi_f = \left|\theta_A - \sin^{-1}\left(R_i^2\sin\left(180 - \delta_y\right)/\overline{C\,O_i}\ \right)\right| \tag{31}$$

$$\phi_g = 180 - \sin^{-1}\left(\overline{C\,O_i}\sin\phi_f / R_i\right) \tag{32}$$

$$\overline{C\,n} = \overline{C\,O_i}\sin(\phi_h)/\sin\left(180 - \left(\phi_f + \phi_g\right)\right) \tag{33}$$

For a slope or flat surface, the following equations were used, respectively:

$$\overline{C\,n} = \left(\overline{C\,s}\sin(90+\gamma)\right)/\sin(90 - \gamma - \theta_A) \tag{34}$$

$$\overline{C\,n} = \overline{C\,s}/\cos\theta_A \tag{35}$$

Finally, the coordinate of n_f was determined by mapping the parametric equation of a cylindrical surface described by Eq. 5 with l_n equal to $\overline{C\,n}$.

5 Obtaining the UE point on the toroidal side

A different method was developed for the UE point on the toroidal side. When it was located on the toroidal side, the UE point can be calculated after its toroidal angle was determined. The method to obtain the toroidal angle of the UE point consists of four steps including two rotations of the reference line using θ_A and θ_B, and the calculation of the inclined radius. The fourth step calculated the toroidal angle of the UE point. All procedures must be performed sequentially, except in certain conditions when it could be skipped, and the next procedure may begin. The method to rotate the reference line for the

engagement point on the cylindrical side and the method to obtain the inclined surface, as presented in section 0, were used. For step 3, although the procedure was similar to the method used for the engagement on the cylindrical surface, the objective was different. The detailed procedure to obtain n_f is derived and discussed in the following sections.

5.1 Rotating the rotated line by θ_A (step 3)

In this procedure, the rotated line, which was obtained in the first rotation by θ_B, was rotated again by θ_A E, even though the final coordinates of the UE point would be obtained in the fourth step. If S_y was a curved surface, then ϕ_g and the length of line $\overline{O_iO_t}$,which are shown in Fig. 7a, were defined in step 3; otherwise, the next procedure was started. The line $\overline{O_iO_t}$ is the distance between the center of the toroidal circle and the center of the workpiece surface (S_i). The angle ϕ_g and the line $\overline{O_iO_t}$ were used as the input for the CWE calculation in step 4. Point O_t is the center point of the toroidal circle and could be located either inside or outside of the workpiece surface. The length of $\overline{b\,O_t}$ was equal to the minor radius of the cutting tool (r), and ϕ_g and $\overline{O_3O_4}$ were calculated using the following equations:

$$\overline{C\,O_i} = \left(\overline{C\,s}^2 + R_i^2 - 2\overline{C\,s}R_i\cos\delta_y\right)^{0.5} \tag{36}$$

$$\phi_f = 180 - |\theta_A| - |\delta_y| + \cos^{-1}\left(\left(\overline{C\,O_i}^2 + R_i^2 - \overline{C\,s}^2\right)/2\overline{C\,O_i}R_i\right) \tag{37}$$

$$\overline{O_iO_t} = \left(\overline{C\,O_t}^2 + \overline{C\,O_i}^2 - 2\overline{C\,O_tC\,O_i}\cos\phi_f\right)^{0.5} \tag{38}$$

$$\phi_g = \sin\left(\frac{\overline{C\,O_i}\sin\phi_f}{\overline{O_iO_t}}\right) \tag{39}$$

5.2 Calculating the toroidal angle of the UE point (step 4)

The UE point (n_f) on the toroidal side was determined by mapping the parametric equation of a toroidal surface. Before the mapping operation was executed, the toroidal angle of the UE point (λ_n) had to be determined. The methods to calculate λ_n for all surface shapes are described below. In this stage, the toroidal cutter was represented as a circle with radius r.

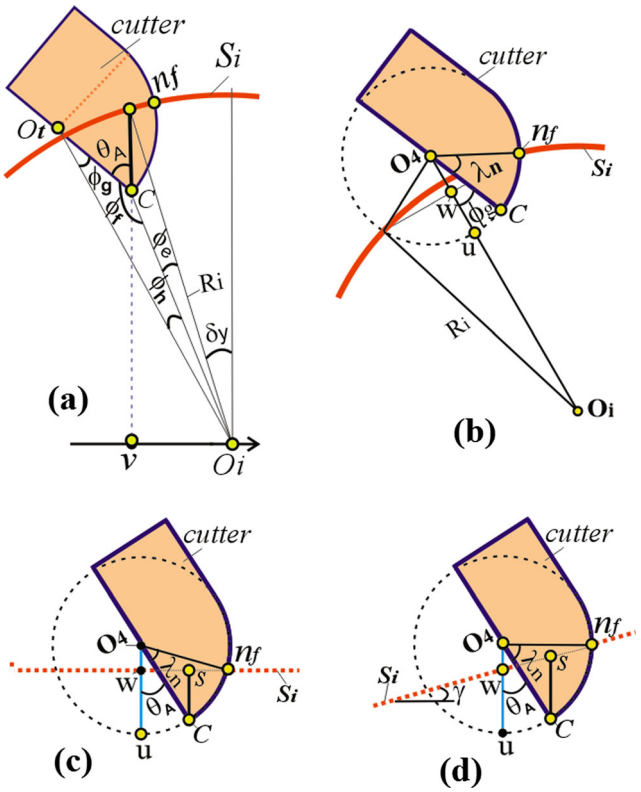

Fig. 7 Procedure to obtain the engagement point on the toroidal side, **a** rotating the rotated line of a curved workpiece surface on S_i, and the intersection between **b** toroidal side and a curved workpiece surface, **c** between the toroidal side and a slope workpiece surface, and **d** between the toroidal side and a flat workpiece surface

6 Curved surface

When the shape of S_i was a curved surface, λ_n was obtained using the intersections of two circles, as shown in Fig. 7b. In this case, the toroidal side of the cutting tool and the workpiece surface were considered to be a circle with a radius r and R_i, respectively. ϕ_g, which was obtained in step 3, was used to define the orientation of the cutting tool. Then λ_n was calculated as follows:

$$\overline{w\,u} = \left(r - r^2 - R_i^2 + \overline{O_iO_t}^2\right)/\left(2\overline{O_iO_t}\right) \tag{40}$$

$$\lambda_n = \cos^{-1}\left(1 - \left(\frac{\overline{w\,u}}{r}\right) + \phi_g\right. \tag{41}$$

7 Flat surface

When S_i was a flat surface, then the two-circle intersection method was not applicable because the workpiece surface could not be represented as a circle. Then, the line λ_n was calculated using Fig. 7c and these equations:

$$\overline{w\,u} = (r - r\cos\theta_2) + \overline{C\,s} \tag{42}$$

$$\lambda_n = \cos^{-1}\left(1 - \left(\frac{\overline{w\,u}}{r}\right) + \theta_2\right. \tag{43}$$

8 Sloped surface

λ_n for a slope surface, as shown in Fig. 7d, was determined using the following equations:

$$\overline{w\,u} = \overline{C\,s} - r(1 + \sin\theta_2 \tan\gamma - \cos\theta_2) \tag{44}$$

$$\lambda_n = 90 - \gamma + \theta_2 - \sin^{-1}\{((r - \overline{w\,u})\sin(90 - \gamma))/r\} \tag{45}$$

Finally, n_f was calculated using the parametric equation of toroidal tool shown in Eq. 6 with $\lambda = \lambda_n$.

After λ_n, λ_C, and l_n were determined, the geometry of the cut was calculated. λ_C is the toroidal angle of the LE point that was calculated using the grazing method discussed in [21]. For a toroidal cutter, l_n was the length of the CWE on the cylindrical side. Therefore, it was equal to zero when n_f was located on the toroidal side. Conversely, when it was on the cylinder side, $\lambda_n = 90$. The length of the cut (L) and the cut thickness (h) were determined using the following equations:

$$L = \frac{\overline{\pi\,r}}{180}(\lambda_n - \lambda_C) + l_n; (\pi = 3.14) \tag{46}$$

$$h = f\cos\alpha\sin\varphi \tag{47}$$

where α is the tool inclination angle and f is the feed rate.

9 Implementation and discussion

Based on the formulae derived in the previous sections, a simulation using MATLAB called the Analytical Boundary Simulation (ABS) was developed. In this section, the proposed method was tested for three types of models with various workpiece surfaces and part surfaces, as shown in Fig. 8. The machining conditions and the cutting tool used for every test are described in Table 1. The ability of the ABS to generate the CWE and the methods used to verify its accuracy are also presented. The efficiency of the proposed method based on computation time was examined by comparing it to that of the Z-mapping method. Finally, the proposed model was used to support the mechanistic cutting force prediction model.

9.1 Cut geometry calculation

Using the developed simulation, the cut shape and length could be calculated. The cut shapes for all test models were generated, as shown in Fig. 8a–c. From these figures, it is shown that the cut shape resembles the shape of the material removed. This indicated that the proposed method was accurate. The length of the cut progression is depicted in Fig. 8d–f. Because the thicknesses of the material removed were relatively constant, the cut lengths produced by all test models were also relatively constant. Smaller cut length at the beginning and end of the CWE, as shown in Fig. 8d, occurred because some part of the cutter was located

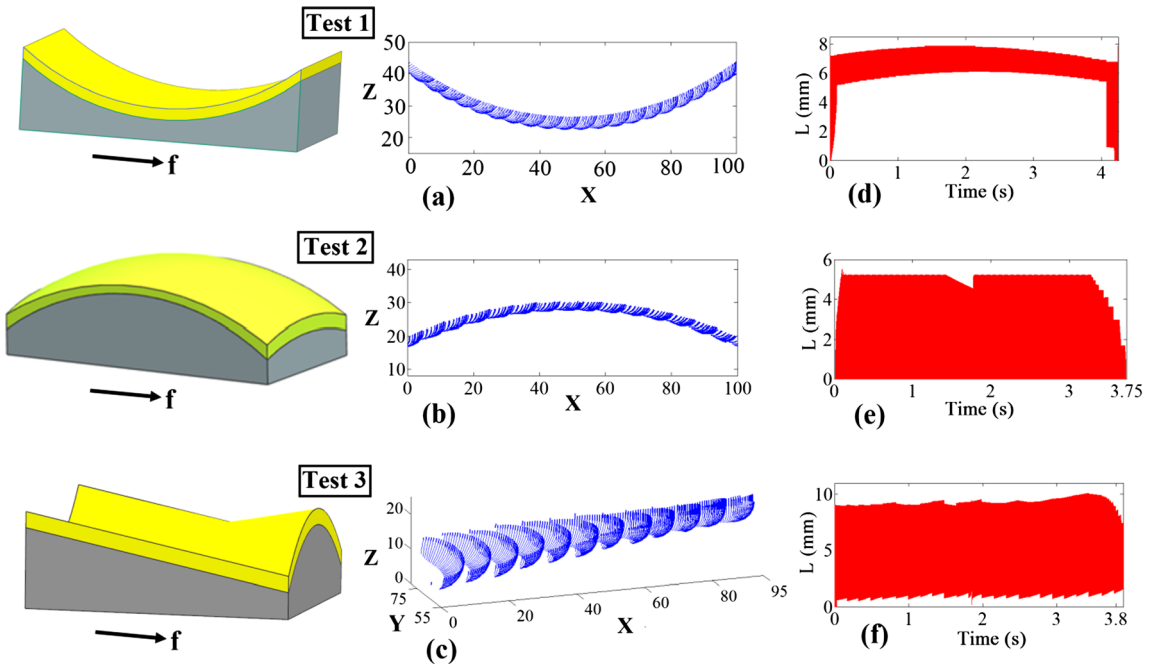

Fig. 8 Test models: **a**–**c** the shape of the cut progressions; **d**–**f** the length of the cut progressions

Table 1 Machining conditions and cutter geometry for every test model

Test No.	Machining conditions		Cutter geometry and orientation		
	Feed rate (mm/tooth)	Cutting speed (rpm)	Diameter (mm)	Minor radius (mm)	Inclination angle
Test 1	0.2	5000	20	5	0
Test 2	0.2	9943	32	4	5
Test	0.2	5000	20	5	10

outside of the workpiece limit when the tool entered or exited the workpiece; this made the CWE smaller and even equal to zero.

The cut shapes as a function of the engagement angle are presented in Fig. 9a–c. Because test 1 was performed without the inclination angle (α), the cut shape at the bottom side was similar to the shape of the cutting tool. However, when the inclination angle was considered, the location of the LE points became dynamic and produced a cut shape that was different from the shape of the cutting tool, as shown in Fig. 9b, c. The cut with a straight and thick line on the top highlighted in Fig. 9c showed that the UE point was located on the cylindrical side. If there were no such line on the top, as highlighted in Fig. 9b, then the UE point would be located on the toroidal side.

The cut lengths as functions of the engagement angle for all test models are presented in Fig. 9d–f. Because the tool was set without the inclination angle in test 1, the CWE on the toroidal side always began at zero. The tool inclination angle made the cut length on the toroidal side always start from zero, as depicted in Fig. 9e; this angle was different from the tool without the inclination angle in which the cut length was larger during the initial engagement.

9.2 Model verification

Although the cut shape resembled the shape of the material removed, the accuracy of the proposed method had to be examined. Verification was performed by comparing the cut lengths calculated using the simulation program with those measured using the commercial software Siemens-NX. As shown in Fig. 10a, the coordinates of the UE point were measured from the extraction model of the intersection between the cutter model and the workpiece model. The extraction model was obtained by placing the cutter model at the instantaneous CC point and adjusting its orientation. Then, the intersection between the cutter model and the workpiece model could be extracted. The cutter was manipulated by making grooves in the front side so that the engagement angle of the CWE could be easily identified. Once

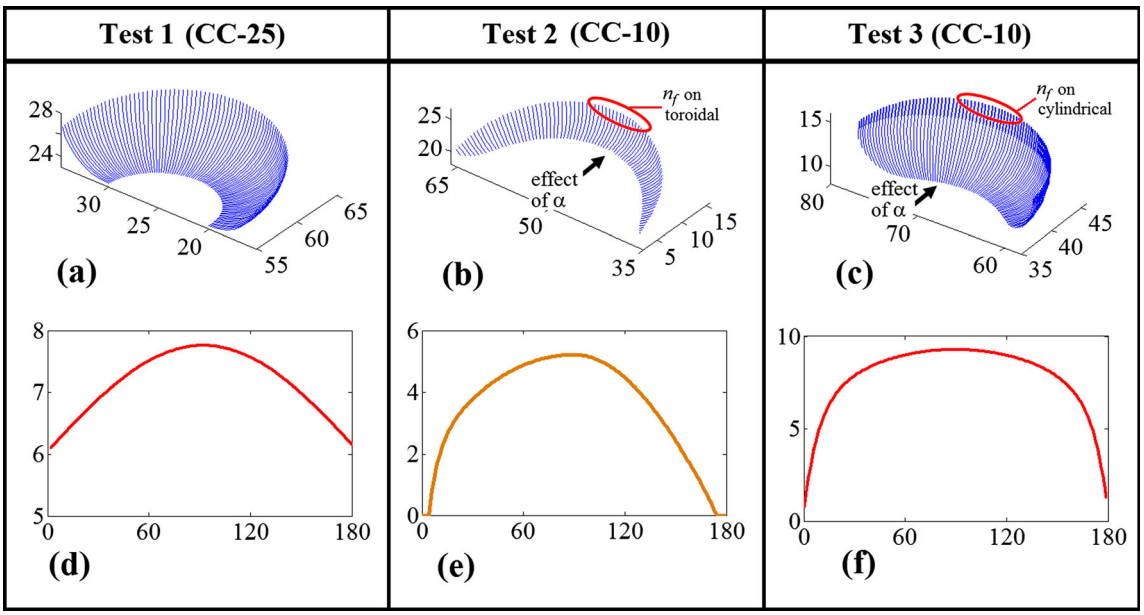

Fig. 9 Shape of the cut geometry, the cut length and the error for $\varphi \in \{0, 180\}$ at selected CC points

the extraction model was obtained, the coordinate of the UE point could be checked, and the cut length could be calculated and compared with those generated by the simulation. The cut lengths for all of the test models shown in Fig. 9 were compared, and the results are shown in Fig. 10b. From these graphs, it is shown that all of the tests produced relatively small errors (i.e., generally less than 6 %); therefore, it can be concluded that the proposed method was accurate.

The accuracy of the proposed model was also verified by comparing the cut geometry obtained from the simulation program with that obtained from the experimental work. For this purpose, a machining test was performed using a Hurco VMX 30U five-axis mill. A two teeth toroidal cutter with a major radius of 6 mm and a minor radius of 2 mm was used as the cutting tool. The cut shape obtained from the experimental work is shown in Fig. 11a, which was captured using a Nikon D5100 digital camera. Because some parts of the cut on the side when the tool entered and exited the workpiece material were damaged, as shown in Fig. 11b, the cut length was only measured in the middle of the cut. For comparison, 36 data points were measured, and the results are shown in Fig. 11c. From this graph, it is shown that there was good agreement between the cut length calculated using the ABS and that measured from the experimental work. In general, the errors were less than 7 %.

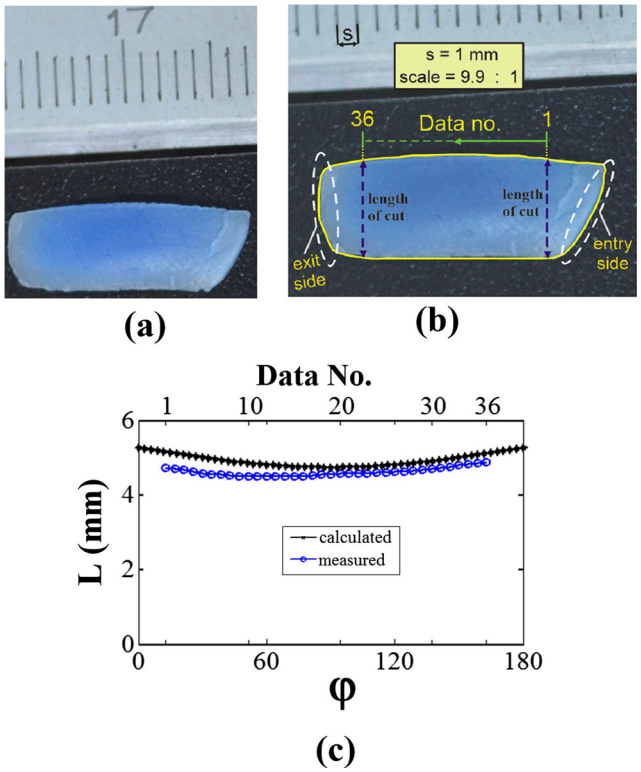

Fig. 11 Experimental verification: **a** cut shape from machining, **b** the length measurement, and **c** the graph of the calculated and measured the cut lengths

9.3 Comparison of the ABS with Z-mapping

To ensure the advantages of the proposed method over a full discretization method, a comparison of computation times was performed; the part and the workpiece model used in test 2 were used in this comparison. For the Z-mapping method, the workpiece surface was discretized with a grid size of 0.1 mm in both the *x*- and *y*-axes.

Both the proposed method and the Z-mapping method were performed using Matlab on an Intel Core i5 1.7 GHz laptop with 6 GB RAM. The uninterrupted test from CC-1 to CC-52 was performed, and the computational time between two consecutive CC points was recorded. This measurement was repeated three times for every method, and the average results are presented in Fig. 12. From this graph, it is shown that the computational time for the ABS is much shorter than the Z-mapping method. The ABS took only 774.05 s to generate the cut length, as shown in Fig. 12, while the Z-mapping took 6589.43 s. The Z-mapping method was thus not a fast algorithm because it must calculate a large amount of surface data. Conversely, the ABS was more efficient because the workpiece surface was defined mathematically.

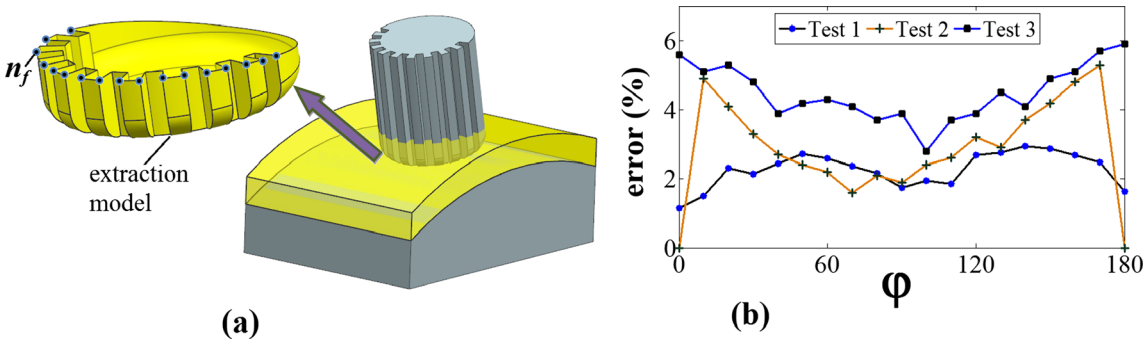

Fig. 10 Model verification: **a** verification method using the Siemens-NX, and **b** the errors of the model test

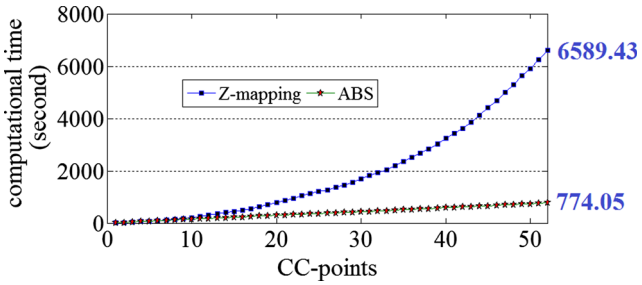

Fig. 12 Comparison of the average computational time between the ABS and Z-mapping methods

9.4 Model implementation in five-axis milling

The proposed cut geometry model was used to support the cutting forces prediction model. The mechanistic cutting force model, which breaks down the cutting force into three components (i.e., tangential, radial, and axial), was used in this study. For the purposes of simulation, the force coefficients (i.e., the cutting and edge coefficients) were determined using the cutting force data that were obtained from a series of experimental studies. A series of full immersion 3D slot milling tests were conducted using a two-tooth carbide end-mill with a 32 mm diameter and a 4 mm minor radius. The machining was performed on a Tripteor X7 five-axis mill, and the cutting forces were measured using a Kistler 9257B three-component dynamometer. The cutting parameters were set as follows: cutting speed = 1000 m/min and a series of axial cut depths of 1, 2, 3.5, 5, 8, and 10 mm. Cutting force coefficients were identified using feed rates 0.1 and 0.3 mm/tooth.

Using these experiments and data processing, the general trend of six cutting and edge force coefficients were determined and are shown in Fig. 13. From this figure, it is shown that the force coefficients fluctuated significantly. The cutting coefficients are shown to be significantly higher than the edge coefficients, which indicate that the shearing force component produced a more significant effect than the total cutting force. From the graph, it can also be observed that the cutting edge coefficients (K_{tc}, K_{rc}, and K_{ac}) have larger variations compared with those of the edge coefficient (K_{te}, K_{re}, and K_{ae}). According to Gao et al. [23], this phenomenon can be explained by the metal removal mechanism acting on the rake and flank contact areas. Significant changes in the cutting coefficients were characterized by the size effect. A larger force coefficient at a smaller axial depth of cut was also found by Erdim et al. [24]. Several studies [25–27] also reported that the cutting force coefficients tend to increase the cut thickness decreases.

For verification, the part and the workpiece for test 2, as shown in Fig. 8, was examined. The cutting force components during one tool pass were measured and compared with the cutting forces calculated by the simulation. Figures 14, 15, and 16 show that the calculated and measured cutting force components agree; in general,

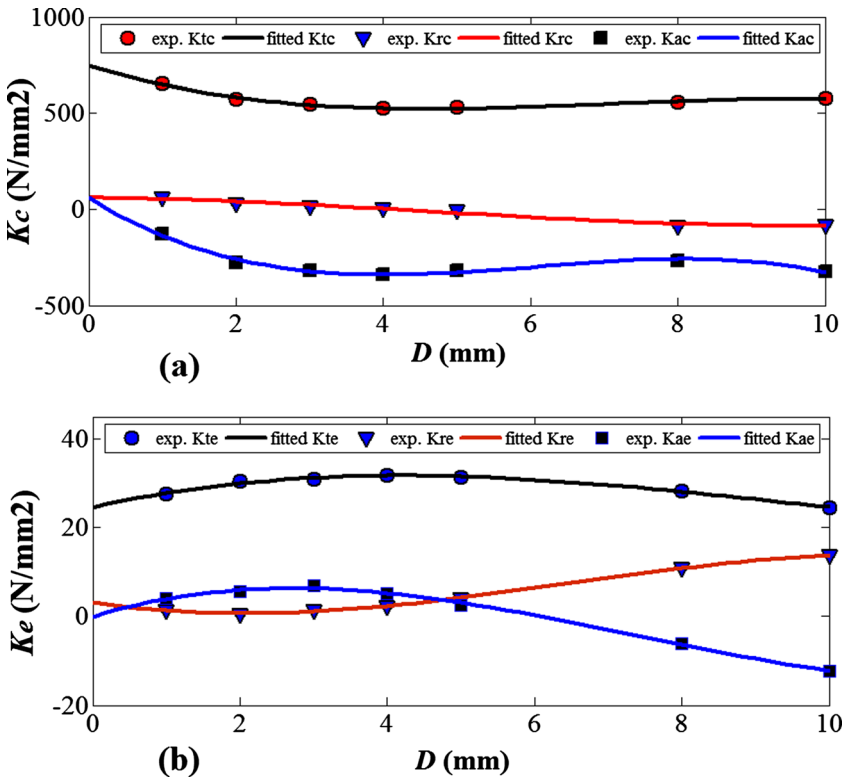

Fig. 13 Force coefficients as a function of axial cut depth: **a** cutting coefficients and **b** edge coefficients

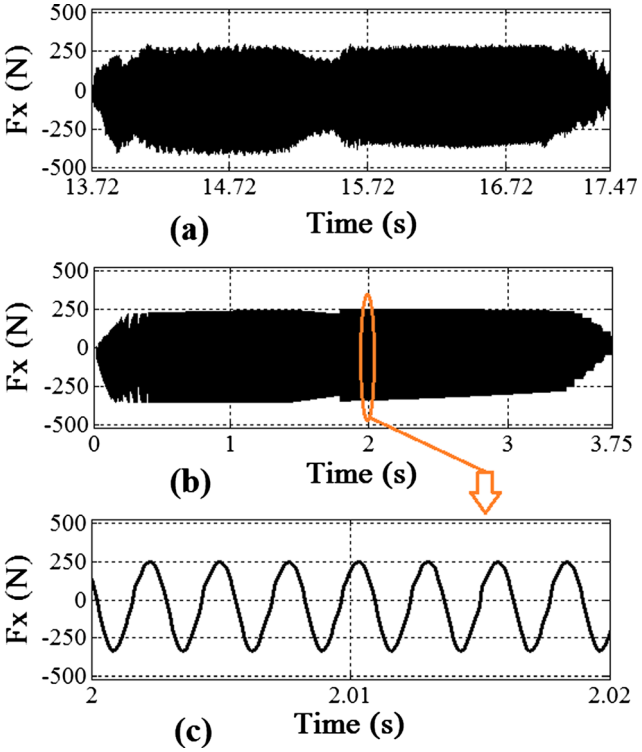

Fig. 14 Comparison of Fx: **a** measured, **b** calculated, and **c** detail of the predicted values

the differences between the simulated and experimental force amplitudes were below 10 %.

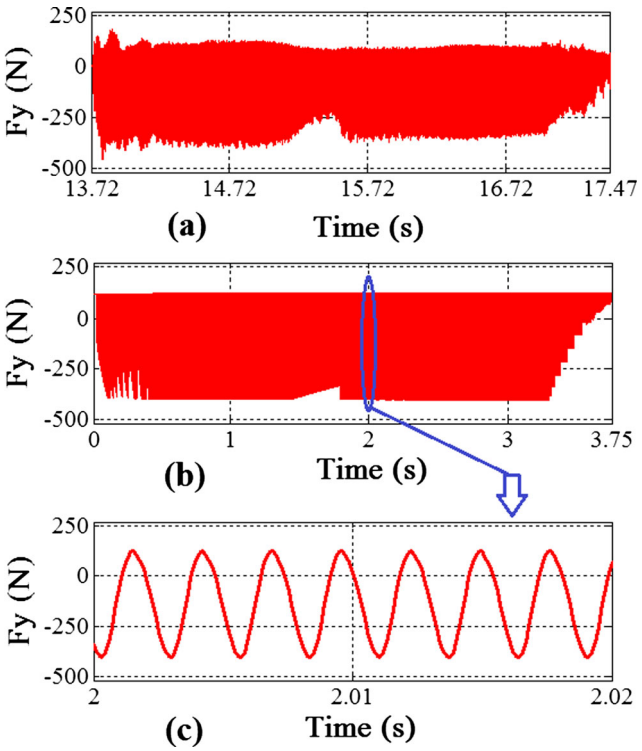

Fig. 15 Comparison of Fy: **a** measured, **b** calculated, and **c** detail of the predicted values

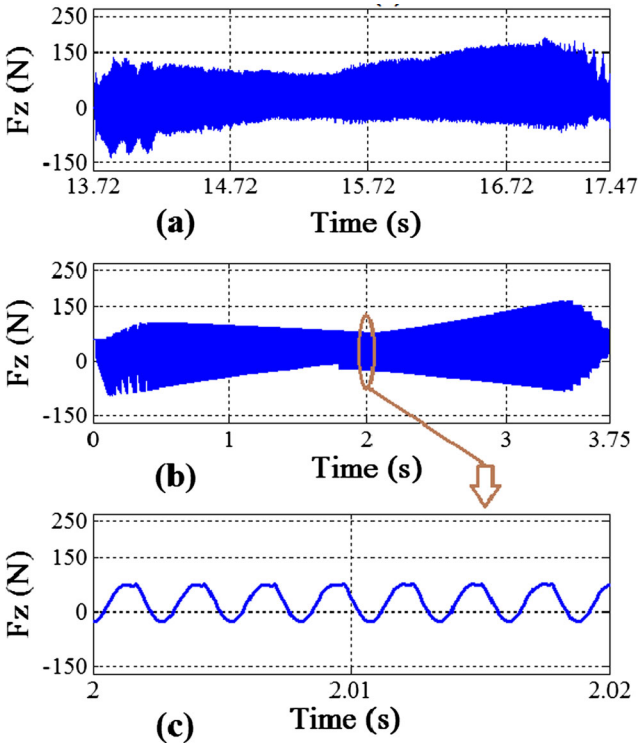

Fig. 16 Comparison of Fz: **a** measured, **b** predicted, and **c** detail of the predicted values

10 Conclusions

In this study, a new method, known as the Analytical Boundary Simulation, was developed to generate the CWE for a toroidal cutter during five-axis milling. A hybrid method, which was a combination between a discrete model and an analytical approach, was developed. The primary contributions of this study include the follow:

1. The ABS is applicable to calculate the chip geometry of a five-axis milling process. This was validated using various parts of a model with different surface profiles.
2. The method was shown to eliminate the need to define the workpiece surface with a large number of discrete vectors. A comparison proved that the ABS was computationally more efficient than the Z-mapping method.
3. The verification tests proved that ABS is accurate; this was verified twice, first by comparing the cut lengths obtained using the ABS with those measured using the Siemens-NX machine, and the second was performed by comparing the cut length calculated using the ABS with the cuts obtained experimentally.
4. The proposed method can be used to support the cutting force prediction model. The validation test showed that the predicted cutting forces show good agreement, both in their trends and amplitudes, with the cutting force generated from the experimental work.

References

1. Liu XW (1995) Five-axis NC cylindrical milling of sculptured surfaces. Comput Aided Des 27(12):887–894
2. El-Mounayri H, Spence AD, Elbestawi MA (1998) Milling process simulation—a generic solid modeller based paradigm. J Manuf Sci Eng 120(2):213–221
3. Ko JH, Yun WS, Cho D W, Ehmann KF(2002) Development of a virtual machining system, part 1: approximation of the size effect for cutting force prediction. International Journal of Machine Tools and Manufacture42(15), 1595–1605.
4. Yun WS, Ko JH, Cho DW, Ehmann KF (2002) Development of a virtual machining system, part 2: prediction and analysis of a machined surface error. Int J Mach Tools Manuf 42(15):1607–1615
5. Merdol SD, Altintas Y (2008) Virtual cutting and optimization of three axis milling processes. Int J Mach Tool Manuf 48(10):1063–1071
6. Kurt M, Bagci E (2011) Feedrate optimisation/scheduling on sculptured surface machining: a comprehensive review, applications and future directions. Int J Adv Manuf Technol 55(9–12):1037–1067
7. Altintas Y, Spence A, Tlusty J (1991) End milling force algorithms for CAD systems. CIRP Ann-Manuf Technol 40(1):31–34
8. Spence AD, Altintas Y (1994) A solid modeler based milling processs simulation and planning system. Trans ASME J Eng Ind 116(1):61–69
9. Fleisig RV, Spence AD (2005) Technique for accelerating B-rep based parallel machining simulation. Comput Aided Des 37(12):1229–1240
10. Jerard RB, Drysdale RL, Hauck K, Schaudt B, Magewick J (1989) Methods for detecting errors in sculptured surface machining. IEEE Comput Graph Appl 9:26–39
11. Park JW, Shin YH, Chung YC (2005) Hybrid cutting simulation via discrete vector model. Comput Aided Des 37(4):419–430
12. Lazoglu I (2003) Sculptural surface machining: a generalized model of ball-end milling force system. Int J Mach Tools Manuf 43(5):453–462
13. Kim GM, Chu CN (2004) Mean cutting force prediction in ball-end milling using force map method. J Mater Process Technol 146(3):303–310
14. Jeong J, Kim K (1999) Generating tool paths for free-form pocket machining using z-buffer-based Voronoi diagrams. Int J Adv Manuf Technol 15(3):182–187
15. Weinert K, Zabel A, Ungemach E, Odendahl S (2008) Improved NC path validation and manipulation with augmented reality method. Prod Eng 2(4):371–376
16. Zhang X, Yu T, Wang W (2014) Modeling, simulation, and optimization of five-axis processes. Int J Adv Manuf Technol 74:1611–1624
17. Lee HU, Cho DW(2003) An intelligent feedrate scheduling based on virtual machining. International Journal of Advanced Manufacturing Technology 22:873–882
18. Ozturk B, Lazoglu I (2006) Machining of free-form surfaces. Part I: analytical chip load. Int J Adv Manuf Technol 46(7):728–735
19. Song G, Li J, Sun J (2013) Approach for modeling accurate undeformed chip thickness in milling operation. Int J Adv Manuf Technol 68(5–8):1429–1439
20. Tunc LT, Budak E (2009) Extraction of 5 axis milling conditions from CAM data for process simulation. Int J Adv Manuf Technol 43(5–6):538–550
21. Kiswanto G, Hendriko H, Duc E (2014) An analytical method for obtaining cutter workpiece engagement during a semi-finish in five-axis milling. Comput Aided Des 55:81–93
22. Gupta SK, Saini SK, Spranklin BW, Yao Z (2005) Geometric algorithms for computing cutter engagement functions in 2.5D milling operations. Comput Aided Des 37(14):1469–1480
23. Gao G, Wu B, Zhang D, Luo M (2013) Mechanistic identification of cutting force coefficients in bull-nose milling process. Chin J Aeronaut 26(3):823–830
24. Erdim H, Lazoglu I, Ozturk B (2006) Feedrate scheduling strategies for free-form surfaces. Int J Mach Tools Manuf 46(7):747–757
25. Wan M, Zhang WH, Qin GH, Tan G (2007) Efficient calibration of instantaneous cutting force coefficients and runout parameters for general end mills. Int J Mach Tools Manuf 47(11):1767–1776
26. Yun WS, Cho DW (2001) Accurate 3-D force prediction using cutting condition independent coefficients in end milling. Int J Adv Manuf Technol 41(4):463–478
27. Denkena B, Vehmeyer J, Niederwestberg D, Maaß P (2014) Identification of the specific cutting force for geometrically defined cutting edges and varying cutting conditions. Int J Mach Tools Manuf 82:42–49